INVESTMENT CASTING OF Cr–Si ALLOYS WITH LIQUIDUS TEMPERATURES UP TO 1900 °C

Kilian Sandner
Metals and Alloys, University of Bayreuth, 95447 Bayreuth, Germany
Department of Materials Science and Engineering, National Tsing Hua University, Hsinchu 30013, Taiwan

Rainer Völkl, Daniel Dickes and Uwe Glatzel
Metals and Alloys, University of Bayreuth, 95447 Bayreuth, Germany

Jyun-Ting Kuo
Department of Materials Science and Engineering, National Tsing Hua University, Hsinchu 30013, Taiwan

An-Chou Yeh
Department of Materials Science and Engineering, National Tsing Hua University, Hsinchu 30013, Taiwan
High Entropy Materials Center, National Tsing Hua University, Hsinchu 30013, Taiwan

https://doi.org/10.1007/s40962-024-01490-7

Abstract

In previous studies, chromium–silicon-based alloys have shown promising material properties for high-temperature applications. For chromium–silicon alloys to be processed on a large scale, primary shaping processes must be adapted to the requirements of these alloys. In this work, binary chromium–silicon alloys are primarily shaped using an investment casting process. Ceramic shell molds made of hafnium oxide stabilized zirconium oxide are developed to withstand the thermal, mechanical and chemical stresses resulting from pouring melts with liquidus temperatures of up to 1900 °C. The layered construction of the shell molds leads to a sufficient thermal shock stability. Energy-dispersive X-ray spectroscopy shows that chemical interactions between the shell mold and the melt do not occur, nor oxides are formed to a detectable extent. Microstructure investigations reveal that casting binary chromium–silicon alloys lead to a coarse grain structure with grain diameters above 300 µm. Strength-increasing precipitations of the intermetallic phase Cr_3Si (A15 phase) can be detected from a silicon content of seven-atom percent in the as-cast state.

Keywords: *castability, Cr–Si alloy, vacuum induction casting*

Introduction

Nickel-based superalloys are currently used for hot parts in stationary gas turbines and aircraft engines.[1] These superalloys have a maximum operating temperature of around 1100 °C. The melting point of the base metal nickel is 1455 °C. To further increase the energy efficiency of turbines, new high-temperature materials with higher maximum operating temperatures are anticipated.[2]

Alloys based on the refractory metals chromium, molybdenum, niobium and others are potential materials for operating temperatures above those of nickel-based superalloys.[2,3] The decision to use in internal combustion engines is good oxidation resistance, high creep resistance, low density and ductile material behavior over the entire operating temperature range[2] as well as processability in complex-shaped parts like turbine blades. Molybdenum-based alloys have good creep properties but most Mo-alloys show catastrophic oxidation behavior above 650 °C.[4,5] Niobium-based alloys also show good creep properties but generally have high densities.[6]

Received: 19 June 2024 / Accepted: 10 October 2024
Published online: 29 December 2024

Chromium-based alloys are characterized by moderate creep properties, good oxidation resistance up to 900 °C as well as an acceptable density and moderate material costs.[7,8] Previous studies have shown that chromium-based alloys can be precipitation hardened and therefore both, the creep and oxidation behavior can be improved.[9] Chromium-based alloys are therefore potential high-temperature materials "Beyond Nickel-Based Superalloys."

A variety of primary shaping processes for refractory-based alloys are reported. A classic powder metallurgical route is described by Zhang et al. and Eck et al.[10,11] Additive manufacturing[12,13] is an alternative; however, for these processes, fine powder of the reactive chromium-based alloys is prerequisite. Gravity die-casting of a chromium-based melt into a cold metallic permanent mold is already applied by the authors. All these primary shaping techniques result in a fine-grained structure which has inherently inferior creep strengths to coarse grain structures. This relationship between grain size and creep strength is generally valid for high-temperature alloys because a fine-grained structure exhibits increased grain boundary diffusion at high temperatures due to the increased grain boundary fraction, thereby reducing the creep strength.[14] Carefully controlled zone melting can result in single crystalline ingots;[15] however, this technique is limited to cylindrical geometries with diameters and length up to 10 and 60 mm, respectively.

Investment casting can result in coarse grain structure and geometrically complex ingots. However, several challenges arise when casting reactive alloys with high liquidus temperatures. On the one hand, the ceramic shell molds must withstand the melt with high liquidus temperature and must have the thermal shock stability to prevent the shell mold from breaking during pouring. In addition, the shell mold material should not chemically interact with the alloy melt to avoid altering the alloy composition. In addition, the process atmosphere must be chosen correctly to hinder volatile alloy elements from evaporating. Due to their strong ionic bonding, oxide ceramics have high-melting points and are therefore most suitable as crucible and shell mold materials, respectively.[16]

In this work, a proprietary investment casting process for high Cr containing Cr–Si alloys is investigated. Compositions of ceramics, shell sequence and process parameters suitable for casting Cr–Si alloys with liquidus temperatures up to 1900 °C are determined.

Experimental

In this work, three binary Cr–Si alloys: $Cr_{98}Si_2$, $Cr_{93}Si_7$ and $Cr_{89}Si_{11}$ (in at. %) are examined. According to the phase diagram, Figure 1,[17] $Cr_{98}Si_2$ (in at.%), is expected to be a single-phase solid solution. The alloys $Cr_{93}Si_7$ and $Cr_{89}Si_{11}$ (in at. %) are expected to be two-phase below about 1200 °C and 1500 °C, respectively, thus enabling precipitation strengthening by the A15 ordered phase Cr_3Si. Table 1 lists the liquidus- and solidus temperatures.

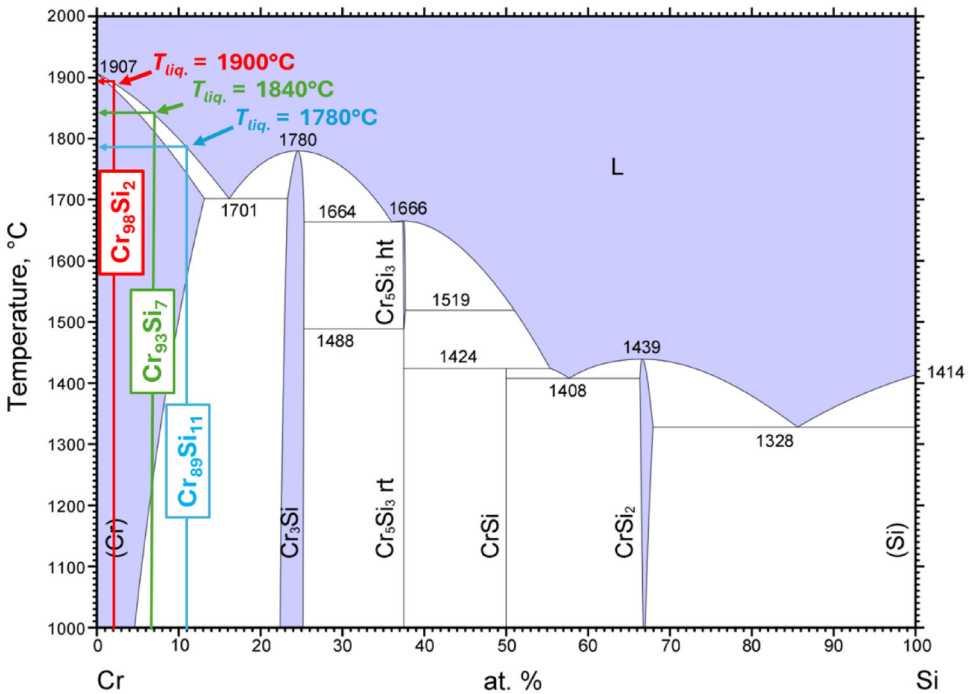

Figure 1. Phase diagram for Cr–Si according to[17] Three compositions investigated in this work are marked.

Table 1. Solidus and Liquidus Temperatures for the Alloys Investigated According to Okamoto[17]

Alloy	Solidus temperature T_s in °C	Liquidus temperature T_l in °C	Comment
$Cr_{98}Si_2$	1890	1900	Single-phase
$Cr_{93}Si_7$	1820	1840	Two phases below 1200 °C
$Cr_{89}Si_{11}$	1750	1780	Two phases below 1500 °C

Elemental Cr used has a purity of 99.995 % while elemental silicon has a purity of 99.95 %. The crucible is selected according to the following criteria (in descending order of priority): thermal shock stability, maximum operating temperature and availability. Approximately 300 g of pure charge elements are placed in magnesium oxide stabilized zirconium oxide crucibles (ZrO_2–MgO-stab.) from Zircoa® (crucible S-2-3.6, flat bottom) and induction melted under argon atmosphere ($p_{Ar} \approx 55$ kPa). The Ar atmosphere is to prevent Cr evaporation. Due to the induced eddy currents, flows arise in the melt, which homogenizes it and thus make the creation of master alloys (e.g., in an arc furnace) unnecessary.

Figure 2 shows the geometry of wax pattern and shell molds. This geometry is used by default for in-house casting. The SX selector is used for single crystal solidification, but single crystal solidification is not the aim of this work. It is therefore only mentioned for the sake of completeness. The wax patterns are created using silicone molds in which melted wax is poured in. The silicone molds are produced by additive manufactured replicas of the final sample geometry. The shell mold green bodies are fabricated in a laboratory scale foundry shop by alternating dipping the wax pattern into a ceramic slurry and successive application of ceramic sand intermittent by air drying. The raw shell molds are finally dried in air for 48 h and then dewaxed in an autoclave (Systec® V-40). The wax free shell mold green bodies are sintered in a chamber furnace (Nabertherm N 100E) according to the temperature profile as shown in Figure 3.

Figure 4 shows a schematic drawing of the vacuum induction furnace used. The shell molds are preheated to a temperature of 1500 °C to minimize thermal shock during casting. To test the chemical and thermal stability of the ceramic material, the shell mold is kept in the heating zone after pouring at 1500 °C for 2 h.

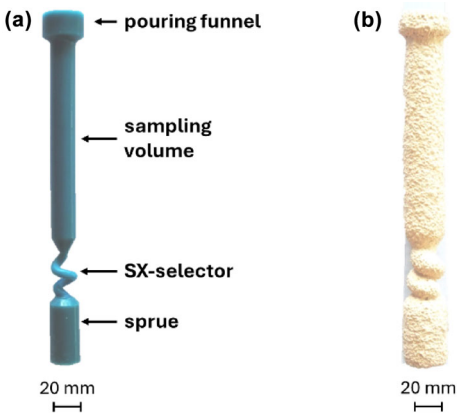

Figure 2. Geometry of wax pattern and ceramic shell mold used in this work: (a): wax pattern and (b): ceramic shell mold.

The cast metal part can be revealed by carefully smashing the shell mold. Any remaining shell mold residues are removed from the specimen using sand blasting.

Three cross-sections are cut from cast ingots and embedded in electrically conductive, graphite containing polymer using a hot embedding press (QATM® Opal X Press). Cross-sections are gradually ground using a wet grinding machine (QATM® QPol 250) with diamond grinding paper with grit sizes up to 2400. Thereafter, the samples are gradually polished with a grain size of 9, 6 and 3 µm. The final polishing step involves polishing with silicon oxide particles with grain size of 0.05 µm in an aqueous suspension. After each polishing step, the samples are cleaned in an ultrasonic bath with ethanol.

The cross-sectional samples are examined by optical microscope (Zeiss® Axioplan 2). Elemental compositions are examined using a micro-X-ray fluorescence analyzer (µXRF) *Orbis PC* system from Ametek®. Phases appearing in the cross-sections are analyzed using a Bruker® D8 Discover X-Ray diffractometer with a Bragg-Brentano setup and a Cu–$K_{\alpha I}$ radiation source. To reduce the Cr fluorescence effect, the lower discriminator setting is adjusted accordingly. The grain size and grain orientation are determined using a scanning electron microscope (SEM) (Zeiss ® Sigma 300 VP) and an electron backscatter diffraction detector (EBSD) from EDAX, (Clarity Super). Backscattered electron images (BSE) and secondary electron images (SE) are obtained using a high-resolution SEM (Zeiss® Gemini 300) with EBSD and energy-dispersive X-ray spectroscopy (EDS) detectors (Oxford® Ultimax 40 and Oxford® Symmetry 2, respectively). To detect light elements (oxygen, nitrogen, and carbon) within the cross-sections, electron probe microanalysis (EPMA) is carried out using a JEOL® Hyper Probe JXA-iHP200F equipped with wavelength dispersive X-ray spectroscopy (WDS) detectors.

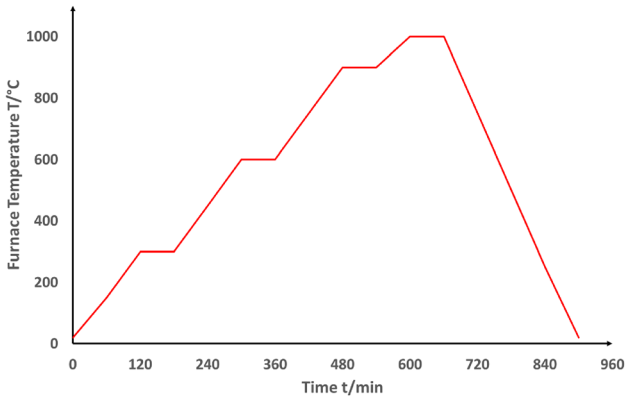

Figure 3. Temperature profile for burning the ceramic shell molds.

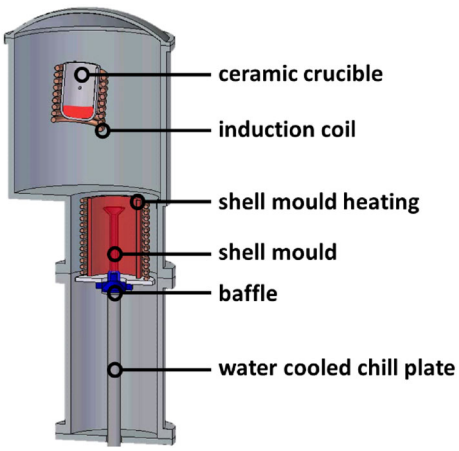

Figure 4. Schematic drawing of the vacuum induction furnace.

Results

Table 2 shows the properties of the final ceramic slurry system used to form the shell mold green bodies. In general, a slurry system consists of four main components: the ceramic powder, the binder, the solvents and additives. After a series of tests, it turned out that additives are not necessary here. The shell molds consist of a total of nine layers that build on each other. Slurry and sand alternate in layers, with the innermost layer (layer 1) consisting of slurry. Zirconium sand is used for layers 2, 4 and 6, while quartz sand is used for the penultimate layer. The outermost layer of the shell molds (layer 9) consists of slurry. Table 3 shows the properties of the sands used. The main component of quartz sand is SiO_2.

Figure 5 shows the shell molds and cast ingots. Some shell molds are manually coated with boron nitride (BN, EKamold EP from 3M®) before casting, to determine if BN is suitable as a release agent for high-melting Cr–Si alloys. Each BN-coated shell mold is air-dried for 30 min to allow the volatile binders to outgas before the melt is poured into the shell mold. The experimental results show that BN

Table 2. Composition of the Ceramic Slurry Used for the Shell Molds

Ceramic slurry system		
	Specifications	Proportion in slurry (in mass %)
Ceramic powder	Manufacturer: Chilches Materials S.A	70.0
	Product: Microzir®	
	Main components (in mass %)	
	ZrO_2+HfO_2 = 65.9	
	SiO_2 = 32.1	
	Al_2O_3 = 0.3	
	TiO_2 = 0.15	
	Particle size distribution (in μm)	
	d50 = 135 ± 50	
	d97 = 250 ± 50	
Binder	Manufacturer: Kuraray Co. Ltd	29.0
	Product: Poval®	
	Main components: polyvinyl alcohol (PVAL), water	
	Viscosity (in mPa•s) = 28.0	
	Ash content (in vol. %) ≤ 0.09	
Solvent	Ethanol (purity 99.5 mol %)	1.0

decomposes at high temperatures, which leads to gas formation. The outgassing of N_2 significantly degrades the surface quality of the castings, which can be seen in Figure 5a. For this reason, the use of BN is abandoned. Figure 5b shows a crack at the spure of the shell mold for the cast of $Cr_{89}Si_{11}$. This crack occurs while removing the shell mold from the vacuum induction furnace. Figure 5b also shows the cast ingot of $Cr_{89}Si_{11}$ with significant less pores on the surface compared to the cast ingot of Figure 5a.

Optical microscope images from the head areas of both $Cr_{98}Si_2$ and $Cr_{93}Si_7$ alloys casts are given in Figure 6. The bulk of cast ingots generally exhibits low porosities. Table 4 lists the composition of the cast parts on the three cross-sections (bottom, middle and head) according to μXRF measurements. It shows that the Cr- and Si content only varies within a small band alongside the cast ingot. A significant loss of Cr due to evaporation cannot be determined.

The elementary composition of the casts on the three cross-sections created (bottom, middle and head) is shown in Table 4

Table 3. Sand Used for the Shell Molds

Sands				
Name	Product	Composition (in mass %)	Particle size distribution (in μm)	Melting point (in °C)
Quartz sand	Merk™ 31623	$SiO_2 \geq 98.0$ $TiO_2 \leq 0.1$ Chloride (CL) ≤ 0.01	$d_{70} = 200 \pm 50$	1700
Zirconium sand	Haixu Abrasives™ ZIRCONIUM	$ZrO_2+HfO_2 \geq 65.5$ $SiO_2 \geq 32.0$ $Al_2O_3 \leq 0.16$ $Fe_2O_3 \leq 0.10$	$d_{50} = 120 \pm 50$	2300

Figure 7a shows the X-ray diffractogram of the head cross-sections for $Cr_{89}Si_{11}$. Figure 7b shows an enlarged area, to point out that A15 phase (Cr_3Si) can be detected for $Cr_{89}Si_{11}$. Only for $Cr_{98}Si_2$ alloy, no A15 phase can be detected, which agrees with the binary phase diagram in Figure 1. Since all cross-sections are embedded in a carbon-containing polymer mold, a peak for carbon can be found in all diffractograms at $2\theta = 26°$.

Figure 8 shows cross-sectional EBSD images from the middle areas of the cast ingots. All three alloy casts are coarse grained, with average grain sizes for $Cr_{98}Si_2$, $Cr_{93}Si_7$ and $Cr_{89}Si_{11}$ in the order of 200 – 400 μm. For $Cr_{98}Si_2$, the grains are elongated, with the long axis lying radially to the cylindrical cast body. $Cr_{98}Si_2$ (highest liquidus temperature) shows the smallest average grain size of 245 μm, while for Cr93Si7 and Cr89Si11, the average grain size is 370 μm and 310 μm, respectively.

Figure 9 shows the back-scattered electron image (BSE) of $Cr_{98}Si_2$ and EDS mappings for Cr and Si. There is no evidence of the A15 phase. XRD measurements (like Figure 7) confirm that the A15 phase cannot be detected for $Cr_{98}Si_2$. The EDS mappings show a homogeneous distribution of Cr and Si over the investigated area, which suggests a Cr–Si solid solution.

Figure 10 reveals finely distributed Cr_3Si precipitates (A15 phase) alongside the grain boundaries for $Cr_{93}Si_7$. Point measurements by EDS show a Si content of around 25 at. % in the silicon-rich phase, which corresponds to the nominal composition of the A15 phase (Cr_3Si).

Figure 11 shows the EPMA results for $Cr_{98}Si_2$ (highest liquidus temperature). There is no evidence of oxide nor nitride inclusions in the edge zone of the cast body. The cross-section investigated was from the top part of the cast, because oxides and nitrides have a lower density then $Cr_{98}Si_2$ and therefore are most likely found in the upper region of the cast body if formed. Since nitrogen and oxygen are light elements, WDS is chosen for detection.

Finally, Table 5 shows the results of point measurements of the top cross-sections of all three casted compositions. There is no evidence of the presence of impurities (oxides, nitrides, Zr, and Mg) to a significant extent.

Discussion

Previous studies have investigated the powder metallurgical processability of refractory metal-based alloys. Eck et al. show in their work that pure chromium powder can be formed into components by hot isostatic pressing (HIP).[11] Zhang et al. have investigated the microstructure of several refractory high-entropy alloys (RHEA).[10] In their work, they show that these alloys can be processed using spark plasma sintering (SPS), selective laser melting (SLM) and arc melting. It turns out that the achievable grain size for spark plasma sintering is in the range 1–10 μm. Kustas et al. investigate the microstructure of additively manufactured (AM) refractory complex-concentrated alloys (RCCAs).[18] From their work, the average achievable grain diameter by SLM is in the range of 1–100 μm. In this work, the grain size of casts of three binary Cr–Si alloys is determined using EBSD mappings (Figure 8). An average grain size of 245 μm can be achieved for the alloy with the highest liquidus temperature ($Cr_{98}Si_2$), while the average grain size for $Cr_{93}Si_7$ and $Cr_{89}Si_{11}$ is around 370 μm and 310 μm, respectively. The grain sizes achieved here are one to two orders of magnitude larger than those of additively manufactured samples. This large grain size results from a low cooling rate due to shell mold preheating. Moreira et al. show in their work that the cooling rate has a major influence on the microstructure.[19] For their experiments, they use a vacuum induction furnace in which they adjust the cooling rate via the withdrawal speed of the cast ingots from the heating zone. They show that the grain density decreases with decreasing cooling rate. With increasing preheating temperatures, higher grain size can

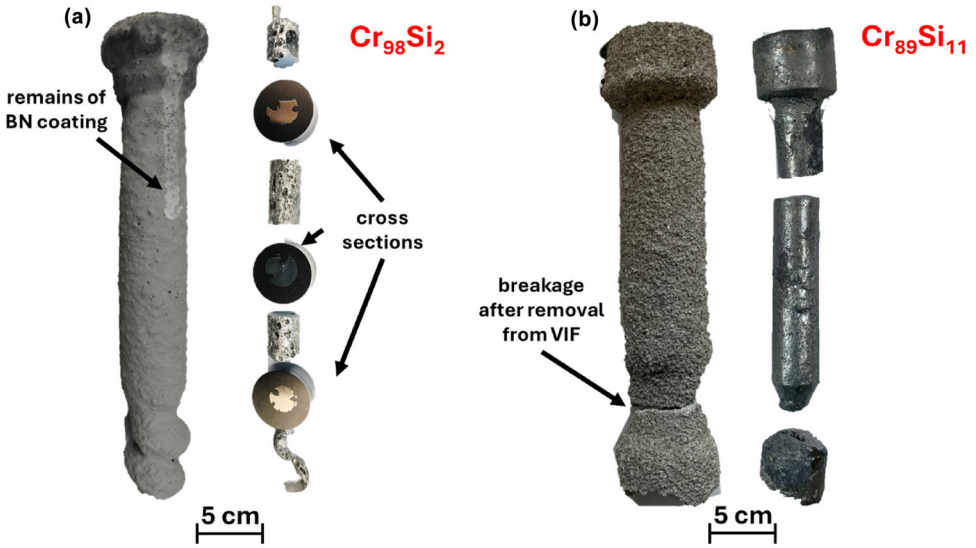

Figure 5. Shell molds containing the cast ingot and cast ingots after demolding. (a) Shell mold with BN coating and demolded cast body for $Cr_{98}Si_2$ (b) Shell mold without BN coating and demolded cast body for $Cr_{89}Si_{11}$.

be achieved. A coarse grain structure is desired for Cr–Si alloys since it generally improves the creep behavior.[9,14]

In case of chemically highly reactive Ti-based alloys, the use of a BN coating of the ceramic shell molds has proven successful in investment casting. It leads to a suppression of chemical and physical interactions between the shell mold material and the melt.[20] In addition, the BN coating facilitates the subsequent demolding of the cast ingot from the shell mold.

In our case of Cr-based alloys, a BN coating of the shell molds is counterproductive, since BN is no longer chemically stable at temperatures above 1800 °C and splits into gaseous N_2 and elemental boron. The formation of gaseous N_2 extremely worsens the surface quality of the cast part, resulting in pores with the size of several mm, see Figure 5a). Hence, BN cannot be used as a shell mold coating when casting Cr–Si alloys.

Table 4. Compositions of the Alloy Ingots According to µXRF Measurements

		Bottom	Middle	Head
$Cr_{89}Si_{11}$	Cr	88.8	88.6	89.7
	Si	11.2	11.4	10.3
$Cr_{93}Si_7$	Cr	93.3	93.1	93.2
	Si	6.7	6.9	6.8
$Cr_{98}Si_2$	Cr	98.3	97.9	98.2
	Si	1.7	2.1	1.8

All given numbers in at.%

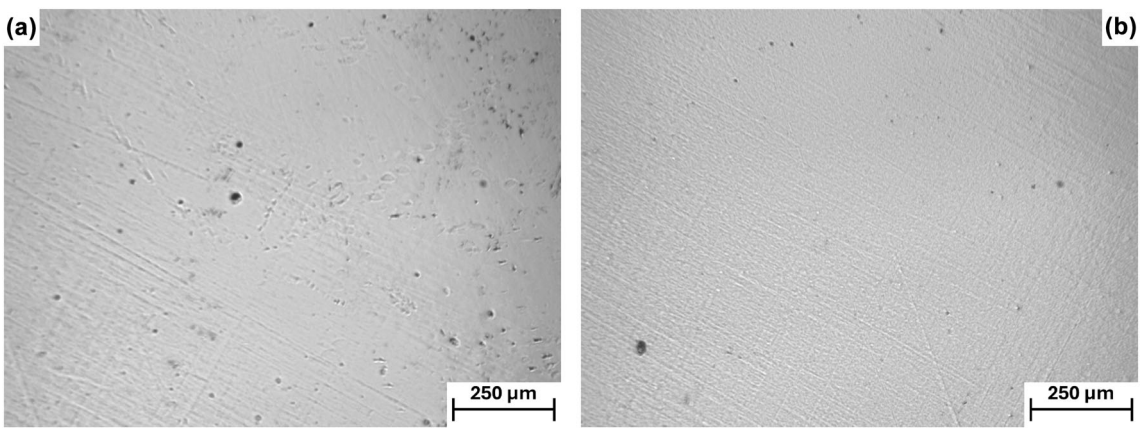

Figure 6. Optical microscope images from the middle of the cross-sections from the heads of two casts: (a) $Cr_{98}Si_2$ and (b) $Cr_{93}Si_7$.

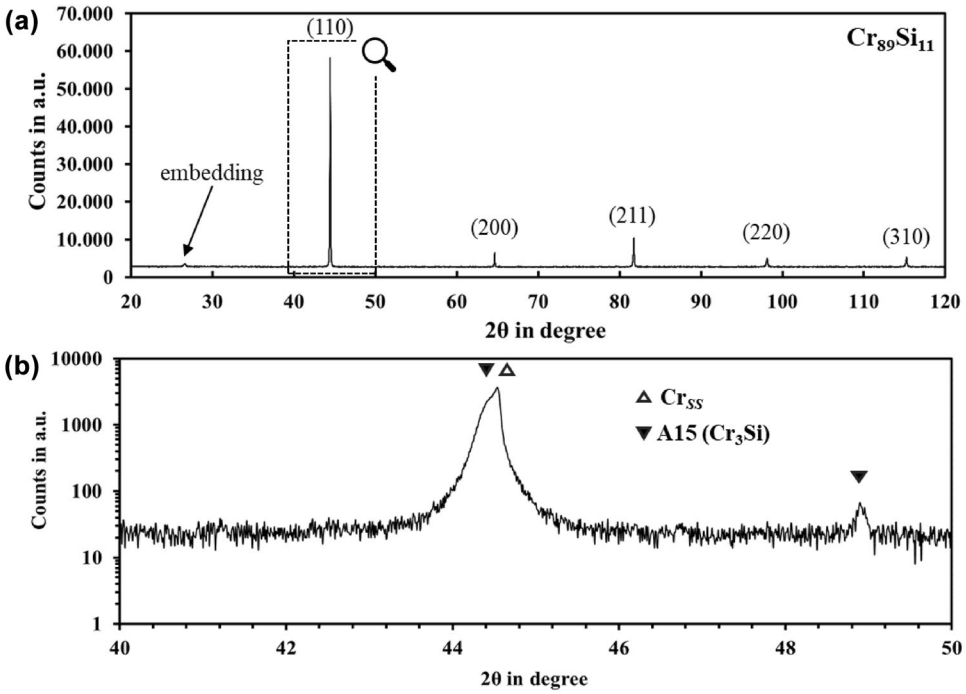

Figure 7. X-ray diffraction (XRD) pattern for $Cr_{89}Si_{11}$: (a) overview and (b) enlarged area to highlight the A15 phase peak.

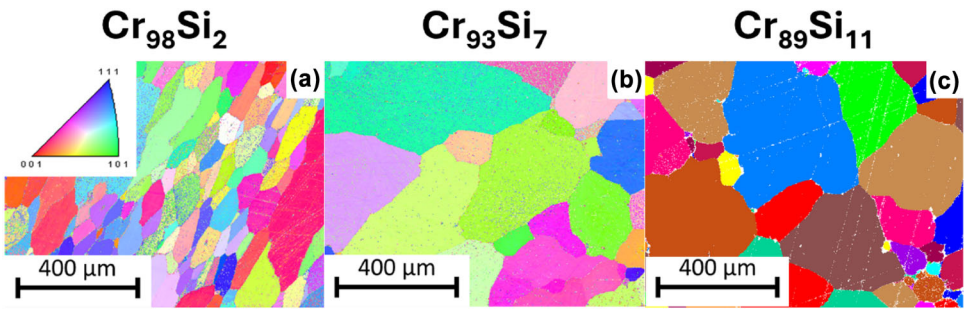

Figure 8. Average grain sizes are estimated from EBSD images. The average grain size is for (a) 245 µm, (b) 370 µm, and (c) 310 µm, respectively.

Chromium tends to evaporate due to its high vapor pressure at elevated temperatures, which changes the alloy composition. In this work, it is shown that by setting an argon atmosphere (p=55 kPa) in the induction furnace during the casting process, chromium vaporization can be successfully reduced. Liu et. al. show that a gaseous atmosphere increases the cooling rate of the cast.[21] An increased cooling rate leads to a faster solidification reducing the chromium vaporization even more. Table 4 shows the alloy composition over the cast bodies and proves the successful suppression of chromium losses.

Precipitations of the A15 phase (Cr_3Si) are crucial for good high-temperature properties of Cr–Si alloys, as Pfizenmaier et al. and Ulrich et al. have shown.[9,22] According to the phase diagram in Figure 1, the solubility of Si in the Cr solid solution is low. A minimum Si content of 5 at. % is

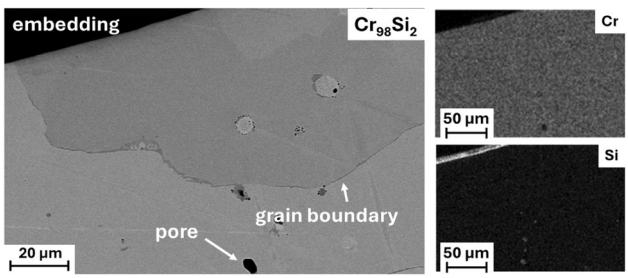

Figure 9. Back-scattered electron (BSE) image of $Cr_{98}Si_2$ with EDS mapping of Cr and Si.

required to form A15 precipitates. The casts of $Cr_{98}Si_2$ consist of a single-phase Cr solid solution. The A15 phase is not detected either by X-ray diffraction or by SEM

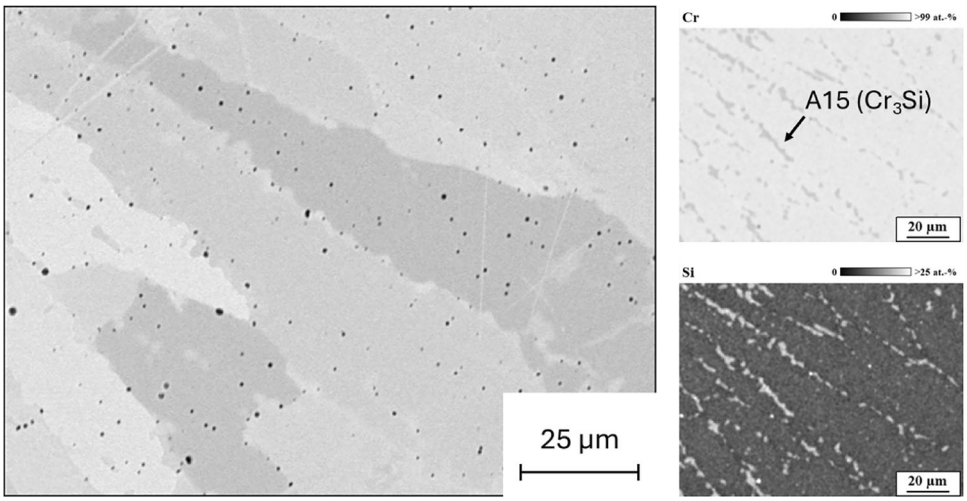

Figure 10. Back-scattered electron (BSE) image of $Cr_{93}Si_7$ with EDS mapping of Cr and Si. Fine Cr_3Si (A15) precipitates occur in the microstructure alongside of grain boundaries.

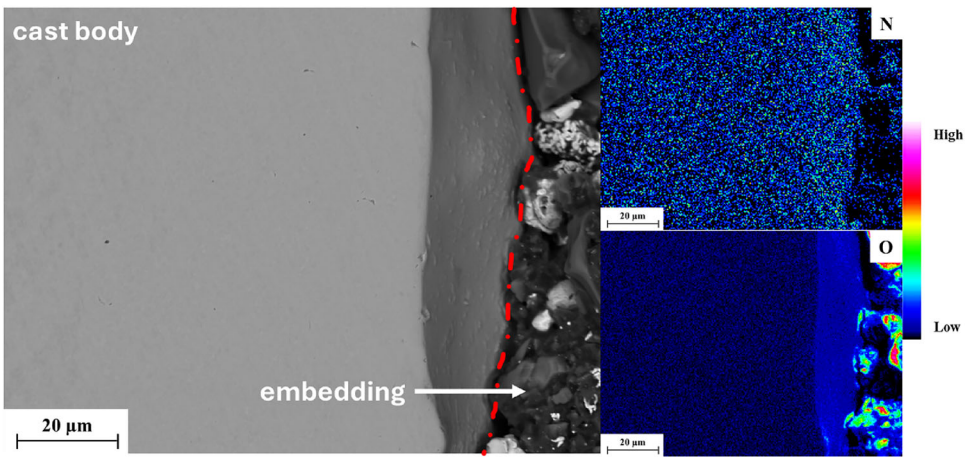

Figure 11. Electron probe micro-analysis (EPMA) results of the edge zone of the $Cr_{98}Si_2$ cast with wavelength dispersive x-ray spectroscopy (WDS) mapping for nitrogen and oxygen.

Table 5. Point Analysis of Elemental Composition of the Top Cross-Sections of all Casts by Using WDS as Method

	Cr	Si	N	O	C	Zr	Hf	Ca
$Cr_{98}Si_2$	98.1	1.9	n.d.	n.d.	n.d.	n.d.	n.d.	n.d.
$Cr_{93}Si_7$	92.8	7.2						
$Cr_{89}Si_{11}$	89.3	10.7						

All numbers given in at.%

n.d. not detectable (lower resolution limit of the detectors 0.5 at.%)

investigations (Figure 9). However, for $Cr_{93}Si_7$ (Figure 10) and $Cr_{89}Si_{11}$ (Figure 7), the A15 phase is detected.

Song et al. show that the high-temperature strength of shell molds depends largely on the back-up sand. The strength of the shell molds can be increased additionally if manufactured automatized instead of handmade.[23] In this work, a successful development of a shell mold system that can both, withstand the thermal stresses when casting high-melting alloys and does not show any significant physical and chemical interactions with the alloy has been made in this work.

Figure 5 shows that the thermal shock stability of the HfO_2-stabilized ZrO_2 shell molds developed in this work is large enough to prevent fatal cracking during pouring. If

chemical or physical interactions occur between the shell mold and the melt, the effects of these interactions can be found in the casting. Both, the XRD measurements (Figure 7) and the elemental analysis (Figure 11 and Table 5) show that no chemical reaction takes place between the melt and the shell mold material during the casting process and the subsequent 2-h holding time at 1500 °C. No oxides or nitrides can be detected in the cast ingot nor can the elements of the shell mold (Zr, Hf and Ca) be detected in the cast bodies when using WDS (Table 5). This shows that binary Cr–Si alloys can be successfully cast in the shell mold system presented in this work and that interactions between the ceramic system and the alloy do not occur to a significant extent.

Conclusions

For the casting of Cr–Si alloys, a ceramic shell mold system based on HfO_2-stabilized ZrO_2 is developed and tested. The shell mold system has the thermal shock stability to pour Cr–Si melts with liquidus temperatures up to 1900 °C. The shell mold system is chemically stable, i.e., no chemical reactions between Cr–Si alloys and the ceramic material are observed. Furthermore, a grain size that is significantly larger than from other processing routes is achieved in our cast samples. A coarse grain structure is anticipated to have better creep and oxidation properties.

Acknowledgements

This work is financed by the German Research Foundation (DFG) through the research project GL 181/60-1, project number 404942487 and by the "High Entropy Materials Center" from The Featured Areas Research Center Program within the framework of the Higher Education Sprout Project by the Ministry of Education (MOE) in Taiwan.

Funding

Open Access funding enabled and organized by Projekt DEAL.

REFERENCES

1. S. Sulzer, M. Hasselqvist, H. Murakami, P. Bagot, M. Moody, R. Reed, The effects of chemistry variations in new nickel-based superalloys for industrial gas turbine applications. Metall. Mater. Trans. A. **51**, 4902–4921 (2020). https://doi.org/10.1007/s11661-020-05845-7
2. J.H. Perepezko, The hotter the engine, the better. Science **326**, 1068–1069 (2009). https://doi.org/10.1126/science.1179327
3. G. Bruzda, W. Polkowski, A. Polkowska, R. Nowak, A. Kudyba, M. Książek, S. Lech, K. Karczewski, D. Giuranno, Mo–Si–B alloys for ultra-high-temperature space and ground applications: liquid-assisted fabrication under various temperature and time conditions. J. Mater. Sci. **57**, 13724–13735 (2022). https://doi.org/10.1007/s10853-022-07457-5
4. Z. Yao, J. Stiglich, T.S. Sudarshan, Molybdenum silicide based materials and their properties. J. Mater. Eng. Perform. **1999**, 291–304 (1999)
5. J.A. Lemberg, R.O. Ritchie, Mo–Si–B alloys for ultrahigh-temperature structural applications. Adv. Mater **24**, 3445–3480 (2012). https://doi.org/10.1002/adma.201200764
6. O.N. Senkov, S.I. Rao, T.M. Butler, T.I. Daboiku, K.J. Chaput, Microstructure and properties of Nb–Mo–Zr based refractory alloys. Int. J. Refract Metal Hard Mater. **92**, 105321 (2020). https://doi.org/10.1016/j.ijrmhm.2020.105321
7. F. Hinrichs, A. Kauffmann, A.S. Tirunilai, D. Schliephake, B. Beichert, G. Winkens, K. Beck, A.S. Ulrich, M.C. Galetz, Z. Long, H. Thota, Y. Eggeler, A. Pundt, M. Heilmaier, A novel nitridation- and pesting-resistant Cr–Si–Mo alloy. Corros. Sci. **207**, 110566 (2022). https://doi.org/10.1016/j.corsci.2022.110566
8. H. Okamoto, Cr–Si phase equilibria. J. Phase Equilib **22**(5), 593–593 (2001)
9. P. Pfizenmaier, A.S. Ulrich, M.C. Galetz, U. Glatzel, Tensile creep properties of Cr–Si alloys at 980 °C in air—influence of Ge and Mo addition. Metals **11**, 1072 (2021). https://doi.org/10.3390/met11071072
10. B. Zhang, Y. Huang, Z. Dou, J. Wang, Z. Huang, Refractory high-entropy alloys fabricated by powder metallurgy: progress, challenges and opportunities. J. Sci.: Adv. Mater. Devices **9**, 100688 (2024). https://doi.org/10.1016/j.jsamd.2024.100688
11. R. Eck, H.P. Martinz, T. Sakaki, M. Kato, Powder metallurgical chromium. Mater. Sci. Eng., A **120–121**, 307–312 (1989). https://doi.org/10.1016/0921-5093(89)90755-7

12. T. Cruse, J. Newkirk, Evaluation of methods to produce tough Cr_3Si based composites. Mater. Sci. Eng., A **239–240**, 410–418 (1997). https://doi.org/10.1016/S0921-5093(97)00611-4
13. B.B. Fernandes, G. Rodrigues, G.C. Coelho, A.S. Ramos, On iron contamination in mechanically alloyed Cr–Si powders. Mater. Sci. Eng., A **405**, 135–139 (2005). https://doi.org/10.1016/j.msea.2005.06.003
14. G. Malakondaiah, R. Rao, Effect of grain size, grain shape and subgrain size on high temperature creep behaviour. Def. Sci. J. **35**, 201–217 (1985)
15. C.-J. Liu, C. Gadelmeier, S.-L. Lu, J.-W. Yeh, H.-W. Yen, S. Gorsse, U. Glatzel, A.-C. Yeh, Tensile creep behavior of HfNbTaTiZr refractory high entropy alloy at elevated temperatures. Acta Mater. **237**, 118188 (2022). https://doi.org/10.1016/j.actamat.2022.118188
16. J.E. Kanyo, S. Schafföner, R.S. Uwanyuze, K.S. Leary, An overview of ceramic molds for investment casting of nickel superalloys. J. Eur. Ceram. Soc. **40**, 4955–4973 (2020). https://doi.org/10.1016/j.jeurceramsoc.2020.07.013
17. H. Okamoto, Cr–Si (chromium-silicon). J. Phase Equilib. **22**, 593 (2001). https://doi.org/10.1361/105497101770332866
18. A.B. Kustas, J. Pegues, M.A. Melia, S.R. Whetten, M. Jones, N. Argibay, Characterization of refractory alloys produced by laser additive manufacturing. Mater. Des. & Process. Commun. **2022**, 1–6 (2022). https://doi.org/10.1155/2022/1928643
19. M.F. Moreira, G.P. Souza, B.N. Venturelli, L.B. Fantin, C.R.F. Azevedo, Effect of the cooling rate on the microstructure of directionally solidified casting (CMSX-4 Ni superalloy). Int. J. Metalcast. **18**, 3292–3312 (2024). https://doi.org/10.1007/s40962-023-01249-6
20. H. Liu, B. Shen, M. Zhu, X. Zhou, X. Mao, Reaction between Ti and boron nitride based investment shell molds used for casting titanium alloys. Rare Met. **27**, 617–622 (2008). https://doi.org/10.1016/S1001-0521(08)60193-X
21. X. Liu, H. Zheng, G. Liu, Z. Guo, Y. Wang, Z. Wang, Investigation and application of inverse determination of interfacial heat transfer coefficient in vacuum investment casting. Int. J. Metalcast. **17**, 1–1 (2024)
22. A.S. Ulrich, P. Pfizenmaier, A. Solimani, U. Glatzel, M.C. Galetz, Strengthened Cr–Si-base alloys for high temperature applications. Int. J. Refract Metal Hard Mater. **76**, 72–81 (2018). https://doi.org/10.1016/j.ijrmhm.2018.05.016
23. Q. Song, X. Zha, M. Ou, C. Lu, J. Li, Y. Ma, High-Temperature flexural strength of aluminosilicate ceramic shells for the investment casting of nickel-based superalloy. Int. J. Metalcast. **18**, 962–974 (2024). https://doi.org/10.1007/s40962-023-01061-2